DQ Impedance Reshaping of Three Phase Power-Controlled Grid Connected Inverter for Low-Frequency Stability Improvement Under Weak Grid Condition

Zhou, Weihua; Wang, Yanbo; E. Torres-Olguin, Raymundo; Chen, Zhe

Published in:
The 12th Annual IEEE Energy Conversion Congress and Exposition (ECCE 2020)

DOI (link to publication from Publisher):
10.1109/ECCE44975.2020.9236052

Publication date:
2020

Document Version
Accepted author manuscript, peer reviewed version

DQ Impedance Reshaping of Three-Phase Power-Controlled Grid-Connected Inverter for Low-Frequency Stability Improvement Under Weak Grid Condition

Weihua Zhou*, Yanbo Wang*, Raymundo E. Torres-Olguin† and Zhe Chen*
*Department of Energy Technology, Aalborg University, Aalborg, Denmark
wez@et.aau.dk, ywa@et.aau.dk, zch@et.aau.dk
†SINTEF Energy Research Institute, Trondheim, Norway
raymundo.torres-olguin@sintef.no

***Abstract*—Phase-locked loop (PLL) is commonly used to synchronize the phase angle of the injected current of voltage source grid-connected inverters (GCIs) with that of the voltage at point of common coupling. However, the quadrature-axis component of the dq impedance model of the GCIs presents negative resistance characteristics in low-frequency range due to the usage of the PLL, which may lead to low-frequency instability phenomena if the GCIs work under weak grid condition. This paper presents a dq impedance reshaping method of power-controlled GCIs to eliminate the negative effect of PLL on low-frequency stability. The dq impedance models of the GCIs under current and power control modes are first established using complex vector and complex transfer function theory. On its basis, the negative effects of PLL on current control loop and power control loop are theoretically derived. A grid voltage feed-forward loop is then designed in the control system of the power-controlled GCIs, where the parameters of the feed-forward loop are calculated. The effectiveness of the proposed dq impedance reshaping method is validated by frequency scanning results and time-domain simulation results.**

***Index Terms*—Grid-connected inverter, impedance reshaping, low-frequency stability, negative resistance, phase-locked loop, power control loop.**

I. Introduction

Renewable energies, such as wind power and solar power, have been increasingly penetrating into utility grid in recent years. Power electronic devices are commonly used as the grid interface to transmit the generated electricity into the utility grid, due to their superior controllability and high efficiency [1]. However, the interactions between multiple-timescale control loops of the grid-connected inverters (GCIs) with time-varying grid impedance tend to cause instability phenomena in wide frequency ranges [2], [3]. Specifically, phase-locked loop (PLL) is commonly used to synchronize the phase angle of the injected grid current with that of the voltage at point of common coupling (PCC) [4]. In addition, outer power control loop is used to regulate the injected active and reactive power. It has widely been reported that low-frequency instability phenomena may occur, if the parameters of the PLL or outer power control loop are not properly designed under weak grid conditions [5]–[11].

The dq impedance model has been reshaped in many works to eliminate the negative resistance characteristics of PLL [7], [9], [12]–[23]. In [7], [9], [12], [13], PLL bandwidth is decreased to narrow the non-passive low-frequency range, which is actually a trade-off between low-frequency stability and system dynamic performance. A robust vector control strategy of the GCI is developed in [14] to eliminate the negative effect of PLL on low-frequency stability under operating point and grid impedance variation, which need not to change the structure and parameters of the standard vector controllers, e.g., power controller, dc-link voltage controller, current controller and PLL. In [15], an improved design of current controller parameters and capacitor-current-feedback coefficient to reduce the negative effect of PLL on current control loop under weak grid condition without additional control strategy is presented. In [16], a symmetric PLL structure is proposed to mitigate the frequency coupling between directional-axis and quadrature-axis impedance components, which can be depicted as a single-input-single-output (SISO) impedance model. The SISO impedance reshaping technique can then be applied for stability enhancement. However, the well-known synchronous reference frame (SRF)-PLL which has an asymmetrical structure is still widely used [7]–[9].

In addition, filter-based impedance reshaping method is presented in [17]–[19]. In [17], notch filter is inserted into PLL control loop to reshape the quadrature-axis impedance, resulting in an enlarged positive resistance region. However, the PLL dynamics tend to be weakened. In [18], band-pass filter is applied to reshape the output impedance of a nearby power converter. However, the impedance is only reshaped at the predetermined frequency points. In [19], the typical delay-based PLL has been improved by adding a second-order

This work was supported by the ForskEL and EUDP project "Voltage Control and Protection for a Grid towards 100% Power Electronics and Cable Network (COPE)" (Project No.: 880063).

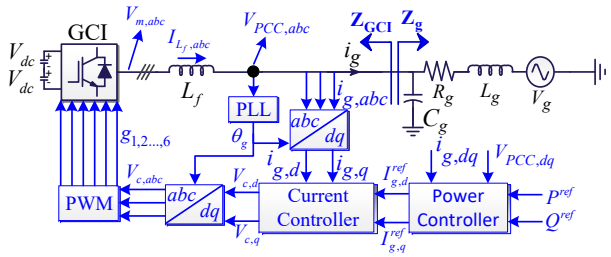

Fig. 1. Control structure of the three-phase GCI with outer power control loop, inner current control loop and PLL.

low-pass filter and a phase correction angle for alleviating the adverse impact of PLLs. It is found in [20], [21] that the phase angle of the q-axis component of the dq impedance model can be boosted by injecting negative reactive power, thus avoiding the low-frequency instability phenomena under weak grid conditions. However, a huge amount of negative reactive power injection may be needed under severely weak grid conditions, which may challenge the maximum capacity of the GCI. In [16], [22]–[24], grid voltage feed-forward control loop is used to reshape the quadrature-axis impedance component. However, only inner current control loop and PLL are investigated in [16], [22], [23], and dc-link voltage control loop is further considered in [24]. Whether the presented dq impedance reshaping method is still effective for power-controlled GCI should further be investigated.

This paper presents a dq impedance reshaping method of power-controlled GCI to mitigate the negative effects of PLL and outer power control loop on low-frequency stability. The dq impedance model of a power-controlled GCI with outer power control loop, inner current control loop and PLL is first established based on complex vectors and complex transfer functions. On its basis, the effects of PLL and outer power control loop on low-frequency impedance characteristics are investigated. A feed-forward control loop is then designed to cancel out the negative effects of PLL and outer power control loop, where the feed-forward coefficient is calculated.

II. Complex Transfer Function-Based DQ Impedance Modeling of PLL

In this section, the typical control structure of the three-phase voltage source GCI is first depicted. On its basis, the dq impedance models considering different control loops are established.

Fig. 1(a) shows the one-line diagram of the three-phase power-controlled GCI. L-type filter L_f is used to attenuate the high-frequency switching harmonics. The grid impedance is emulate as a series inductor L_g and resistor R_g in parallel with a shunt capacitor C_g. SRF-PLL is used to synchronize the phase angle of the PCC voltage with that of the injected grid current. In addition, outer power controller and inner current controller are realized by PI controller in dq reference frame.

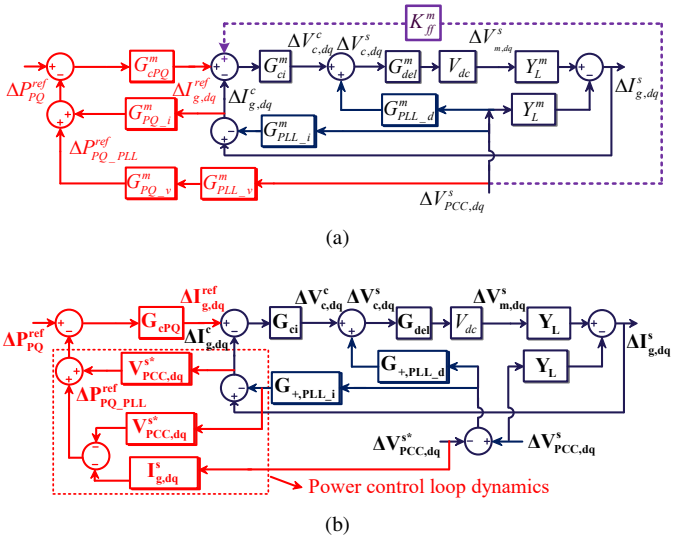

Fig. 2. Block diagram of Fig. 1(a). (a) Based on real space vectors and transfer matrices [9]. (b) Based on complex space vectors and complex transfer functions.

A. Block Diagram Representation Based on Complex Space Vectors and Complex Transfer Functions

The definition of complex space vectors and complex transfer functions can be found in [21], [25], [26]. In addition, how to transfer the real space vectors into complex space vectors and transfer 2×2 transfer matrices into complex transfer functions are also explained in [21], [25], [26]. The block diagram of Fig. 1(a) based on real space vectors and 2×2 transfer matrices has been established in [9], which is shown as the blue part in Fig. 2(a) as a basis to derive the dq impedance model represented in the form of complex space vectors and complex transfer functions. The parameters of current control loop and PLL in Fig. 2(a) can be reformulated as

$$I^{ref}_{g,dq} \rightarrow \mathbf{I^{ref}_{g,dq}} \quad I^{s}_{g,dq} \rightarrow \mathbf{I^{s}_{g,dq}} \quad I^{c}_{g,dq} \rightarrow \mathbf{I^{c}_{g,dq}} \quad V^{s}_{PCC,dq} \rightarrow \mathbf{V^{s}_{PCC,dq}}$$
$$V_{m,dq} \rightarrow \mathbf{V_{m,dq}} \quad V^{c}_{c,dq} \rightarrow \mathbf{V^{c}_{c,dq}} \quad V^{s}_{c,dq} \rightarrow \mathbf{V^{s}_{c,dq}} \tag{1}$$

$$G^m_{ci} = \begin{bmatrix} k_{pi} + \frac{k_{ii}}{s} & 0 \\ 0 & k_{pi} + \frac{k_{ii}}{s} \end{bmatrix} \rightarrow \mathbf{G_{ci}} = k_{pi} + \frac{k_{ii}}{s}$$
$$G^m_{del} = \begin{bmatrix} e^{-1.5sT_s} & 0 \\ 0 & e^{-1.5sT_s} \end{bmatrix} \rightarrow \mathbf{G_{del}} = e^{-1.5sT_s} \tag{2}$$
$$Y^m_L = \frac{1}{L_f(s^2+\omega_1^2)} \begin{bmatrix} s & \omega_1 \\ -\omega_1 & s \end{bmatrix} \rightarrow \mathbf{Y_L} = \frac{1}{L_f(s+j\omega_1)}$$

$$G^m_{PLL\_i} = \begin{bmatrix} 0 & -I^s_{g,q}G_{PLL} \\ 0 & I^s_{g,d}G_{PLL} \end{bmatrix} \rightarrow$$
$$\mathbf{G_{+,PLL\_i}} = -\mathbf{G_{-,PLL\_i}} = \frac{\mathbf{I^s_{g,dq}}G_{PLL}}{2} \tag{3}$$
$$G^m_{PLL\_d} = \begin{bmatrix} 0 & -V^s_{c,q}G_{PLL} \\ 0 & V^s_{c,d}G_{PLL} \end{bmatrix} \rightarrow$$
$$\mathbf{G_{+,PLL\_d}} = -\mathbf{G_{-,PLL\_d}} = \frac{\mathbf{V^s_{c,dq}}G_{PLL}}{2}$$

$$G_{PLL} = \frac{tf_{PLL}}{s + tf_{PLL} V^s_{PCC,d}} \qquad tf_{PLL} = k_{ppll} + \frac{k_{ipll}}{s} \quad (4)$$

where tf_{PLL} is the PI transfer function of PLL controller.

Based on (1)-(3), block diagrams of the GCI considering inner current control loop and PLL are represented using complex space vectors and complex transfer functions, shown as the blue part in Fig. 2(b). The red part for outer power control loop will be investigated in Section III.

B. DQ Impedance Modeling Considering only Current Control Loop

The closed-loop response of $\mathbf{\Delta I^s_{g,dq}}$ when considering only current control lolop can be derived from Fig. 2(b), shown as

$$\mathbf{\Delta I^s_{g,dq}} = \mathbf{G^{CCL}_{cl,dq}} \mathbf{\Delta I^{ref}_{g,dq}} - \mathbf{Y^{CCL}_{cl,dq}} \mathbf{\Delta V^s_{PCC,dq}} \quad (5)$$

where $\mathbf{G^{CCL}_{cl,dq}}$ and $\mathbf{Y^{CCL}_{cl,dq}}$ are the closed-loop gain and output admittance, respectively, shown as

$$\mathbf{G^{CCL}_{cl,dq}} = \mathbf{T_{cl,dq}}/(1 + \mathbf{T_{cl,dq}}) \quad \mathbf{Y^{CCL}_{cl,dq}} = \mathbf{Y_L}/(1 + \mathbf{T_{cl,dq}}) \quad (6)$$

where $\mathbf{T_{cl,dq}} = \mathbf{G_{ci}} \mathbf{G_{del}} V_{dc} \mathbf{Y_L}$ is the open-loop gain.

The dq admittance matrix $Y^{CCL,m}_{dq}$ can be obtained by substituting (2) into (6), shown as

$$\begin{aligned} &\mathbf{Y^{CCL}_{cl,dq}} = \frac{1}{L_f(s + j\omega_1) + G_{ci} G_{del} V_{dc}} \rightarrow \\ &Y^{CCL,m}_{dq} = \begin{bmatrix} Y^{CCL}_{dd} & Y^{CCL}_{dq} \\ Y^{CCL}_{qd} & Y^{CCL}_{qq} \end{bmatrix} \\ &= \frac{1}{\Lambda_1} \begin{bmatrix} L_f s + G_{ci} G_{del} V_{dc} & \omega_1 L_f \\ -\omega_1 L_f & L_f s + G_{ci} G_{del} V_{dc} \end{bmatrix} \end{aligned} \quad (7)$$

where

$$\Lambda_1 = (L_f s + G_{ci} G_{del} V_{dc})^2 + \omega_1^2 L_f^2 \quad (8)$$

On the other hand, when $\mathbf{\Delta I^{ref}_{g,dq}} = 0$, the following equation can be obtained based on (6).

$$\begin{aligned} -\begin{bmatrix} \mathbf{\Delta I^s_{g,dq}} \\ \mathbf{\Delta I^{s*}_{g,dq}} \end{bmatrix} &= \begin{bmatrix} \mathbf{Y^{CCL}_{cl,dq}} & 0 \\ 0 & \mathbf{Y^{CCL*}_{cl,dq}} \end{bmatrix} \begin{bmatrix} \mathbf{\Delta V^s_{PCC,dq}} \\ \mathbf{\Delta V^{s*}_{PCC,dq}} \end{bmatrix} \\ &= \mathbf{Y^{CCL,m}_{\pm,dq}} \begin{bmatrix} \mathbf{\Delta V^s_{PCC,dq}} \\ \mathbf{\Delta V^{s*}_{PCC,dq}} \end{bmatrix} \end{aligned} \quad (9)$$

Then, the dq impedance matrix $Z^{CCL,m}_{dq}$ can be obtained as [26], [27]

$$\begin{aligned} Z^{CCL,m}_{dq} &= A_Z^{-1} \mathbf{Z^{CCL,m}_{\pm,dq}} A_Z \\ &= \begin{bmatrix} L_f s + G_{ci} G_{del} V_{dc} & -\omega_1 L_f \\ \omega_1 L_f & L_f s + G_{ci} G_{del} V_{dc} \end{bmatrix} \end{aligned} \quad (10)$$

where $A_Z = \frac{1}{\sqrt{2}}[1, j; 1, -j]$.

It can be seen from (7) and (10) that the dq impedance models obtained by the two methods are the same.

C. DQ Impedance Modeling Further Considering PLL

When further considering PLL, two more feed-forward paths which consist of $\mathbf{G_{+,PLL\_d}}$ and $\mathbf{G_{+,PLL\_d}}$, respectively, should be considered. The closed-loop response of $\mathbf{\Delta I^s_{g,dq}}$ can then be derived as

$$\begin{aligned} \mathbf{\Delta I^s_{g,dq}} = &\mathbf{G^{CCL}_{cl,dq}} \mathbf{\Delta I^{ref}_{g,dq}} - \mathbf{Y^{CCL}_{cl,dq}} \mathbf{\Delta V^s_{PCC,dq}} \cdots \\ &\underbrace{+\mathbf{Y^{PLL}_{cl,dq}} \mathbf{\Delta V^s_{PCC,dq}} - \mathbf{Y^{PLL}_{cl,dq}} \mathbf{\Delta V^{s*}_{PCC,dq}}}_{\textbf{Effects of PLL dynamics}} \end{aligned} \quad (11)$$

where the detailed expression of $\mathbf{Y^{PLL}_{cl,dq}}$ is shown as

$$\mathbf{Y^{PLL}_{cl,dq}} = \left(\frac{\mathbf{G_{+,PLL\_d}}}{\mathbf{G_{ci}}} + \mathbf{G_{+,PLL\_i}}\right) \mathbf{G^{CCL}_{cl,dq}} \quad (12)$$

When $\mathbf{\Delta I^{ref}_{g,dq}} = 0$, the following equation can be obtained based on (11).

$$\begin{aligned} -\begin{bmatrix} \mathbf{\Delta I^s_{g,dq}} \\ \mathbf{\Delta I^{s*}_{g,dq}} \end{bmatrix} &= \begin{bmatrix} \mathbf{Y^{CCL}_{cl,dq}} - \mathbf{Y^{PLL}_{cl,dq}} & \mathbf{Y^{PLL}_{cl,dq}} \\ \mathbf{Y^{PLL*}_{cl,dq}} & \mathbf{Y^{CCL*}_{cl,dq}} - \mathbf{Y^{PLL*}_{cl,dq}} \end{bmatrix} \cdots \\ &\begin{bmatrix} \mathbf{\Delta V^s_{PCC,dq}} \\ \mathbf{\Delta V^{s*}_{PCC,dq}} \end{bmatrix} = \mathbf{Y^{PLL,m}_{\pm,dq}} \begin{bmatrix} \mathbf{\Delta V^s_{PCC,dq}} \\ \mathbf{\Delta V^{s*}_{PCC,dq}} \end{bmatrix} \end{aligned} \quad (13)$$

Similar with (10), the dq admittance model further considering PLL dynamics can be derived as

$$Y^{PLL,m}_{dq} = \begin{bmatrix} Y^{PLL}_{dd} & Y^{PLL}_{dq} \\ Y^{PLL}_{qd} & Y^{PLL}_{qq} \end{bmatrix} = A_Z^{-1} \mathbf{Y^{PLL,m}_{\pm,dq}} A_Z \quad (14)$$

where

$$\begin{aligned} &Y^{PLL}_{qq} = \frac{\mathbf{Y^{CCL}_{cl,dq}} + \mathbf{Y^{CCL*}_{cl,dq}}}{2} - \mathbf{Y^{PLL}_{cl,dq}} - \mathbf{Y^{PLL*}_{cl,dq}} = \cdots \\ &Y^{CCL}_{qq} - [(V^s_{c,d} + I^s_{g,d} G_{ci})(L_f s + G_{ci} G_{del} V_{dc}) \cdots \\ &-j\omega_1 L_f (V^s_{c,q} + I^s_{g,q} G_{ci})] G_{PLL} G_{del} V_{dc} / \Lambda_1 \end{aligned} \quad (15)$$

It can be seen from (7) and (15) that Y^{PLL}_{qq} are affected by PLL dynamics.

On the other hand, the q-axis impedance component further considering PLL dynamics can be derived as

$$Z^{PLL}_{qq} = Z^{CCL}_{qq} / (1 - (V^s_{c,d} + I^s_{g,d} G_{ci}) G_{PLL} G_{del} V_{dc}) \quad (16)$$

It can be seen from (10) and (16) that, the q-axis impedance component is affected by PLL dynamics.

III. Complex Transfer Function-Based DQ Impedance Modeling of Power Control Loop

In this section, the outer power control loop, i.e., the red part of Fig. 2(a), is further modeled using complex space vectors and complex transfer functions.

A. Reformulation of Control Block Diagram of Fig. 2(a) Using Complex Space Vectors and Complex Transfer Functions

The parameters related with the outer power control loop can be reformulated as

$$P_{PQ}^{ref} = \begin{bmatrix} P^{ref} \\ Q^{ref} \end{bmatrix} \rightarrow \mathbf{P_{PQ}^{ref}} = P^{ref} + jQ^{ref}$$

$$P_{PQ\_PLL}^{ref} = \begin{bmatrix} P_{PLL}^{ref} \\ Q_{PLL}^{ref} \end{bmatrix} \rightarrow \mathbf{P_{PQ\_PLL}^{ref}} = P_{PLL}^{ref} + jQ_{PLL}^{ref}$$

$$G_{cPQ}^{m} = \begin{bmatrix} k_{pPQ} + \frac{k_{iPQ}}{s} & 0 \\ 0 & k_{pPQ} + \frac{k_{iPQ}}{s} \end{bmatrix} \rightarrow$$

$$\mathbf{G_{cPQ}} = k_{pPQ} + \frac{k_{iPQ}}{s}$$

$$G_{PQ\_i}^{m} = \begin{bmatrix} V_{PCC,d}^{s} & V_{PCC,q}^{s} \\ -V_{PCC,q}^{s} & V_{PCC,d}^{s} \end{bmatrix} \rightarrow \mathbf{G_{PQ\_i}} = \mathbf{V_{PCC,dq}^{s*}} \quad (17)$$

and

$$G_{PQ\_v}^{m} = \begin{bmatrix} -I_{g,d}^{s} & -I_{g,q}^{s} \\ -I_{g,q}^{s} & I_{g,d}^{s} \end{bmatrix} \rightarrow$$
$$\mathbf{G_{+,PQ\_v}} = 0 \qquad \mathbf{G_{-,PQ\_v}} = -\mathbf{I_{g,dq}^{s}} \quad (18)$$

$$G_{PLL\_v}^{m} = \begin{bmatrix} 1 & V_{PCC,q}^{s} G_{PLL} \\ 0 & 1 - V_{PCC,d}^{s} G_{PLL} \end{bmatrix} \rightarrow$$
$$\mathbf{G_{+,PLL\_v}} = 1 - \mathbf{V_{PCC,dq}^{s}} G_{PLL}/2$$
$$\mathbf{G_{-,PLL\_v}} = \mathbf{V_{PCC,dq}^{s}} G_{PLL}/2 \quad (19)$$

Note that $G_{PQ\_v}^{m}$ and $G_{PLL\_v}^{m}$ are cascaded in Fig. 2(a). Therefore,

$$G_{PQ\_PLL\_v}^{m} = G_{PQ\_v}^{m} G_{PLL\_v}^{m} =$$
$$\begin{bmatrix} -I_{g,d}^{s} & -I_{g,q}^{s} - I_{g,d}^{s} V_{PCC,q}^{s} G_{PLL} + I_{g,q}^{s} V_{PCC,d}^{s} G_{PLL} \\ -I_{g,q}^{s} & I_{g,d}^{s} - I_{g,q}^{s} V_{PCC,q}^{s} G_{PLL} - I_{g,d}^{s} V_{PCC,d}^{s} G_{PLL} \end{bmatrix} \rightarrow$$
$$\mathbf{G_{+,PQ\_PLL\_v}} = -\frac{\mathbf{I_{g,dq}^{s}} \mathbf{V_{PCC,dq}^{s*}}}{2} G_{PLL}$$
$$\mathbf{G_{-,PQ\_PLL\_v}} = -\mathbf{I_{g,dq}^{s}} + \frac{\mathbf{I_{g,dq}^{s}} \mathbf{V_{PCC,dq}^{s*}} G_{PLL}}{2} \quad (20)$$

By combining (3) and (20), the following equation can be obtained.

$$\mathbf{G_{+,PQ\_PLL\_v}} = -\mathbf{G_{+,PLL\_i}} \mathbf{V_{PCC,dq}^{s*}}$$
$$\mathbf{G_{-,PQ\_PLL\_v}} = -\mathbf{I_{g,dq}^{s}} + \mathbf{G_{+,PLL\_i}} \mathbf{V_{PCC,dq}^{s*}} \quad (21)$$

The following equation can then be obtained from Fig. 2(a).

$$\mathbf{\Delta P_{PQ\_PLL}^{ref}} = \mathbf{G_{+,PQ\_PLL\_v}} \mathbf{\Delta V_{PCC,dq}^{s}} + \mathbf{G_{-,PQ\_PLL\_v}} \cdots$$
$$\mathbf{\Delta V_{PCC,dq}^{s*}} = -\mathbf{I_{g,dq}^{s}} \mathbf{\Delta V_{PCC,dq}^{s*}} - \mathbf{G_{+,PLL\_i}} \mathbf{V_{PCC,dq}^{s*}} \cdots$$
$$(\mathbf{\Delta V_{PCC,dq}^{s}} - \mathbf{\Delta V_{PCC,dq}^{s*}}) \quad (22)$$

Based on (22), the small-signal model of the outer power control loop can be represented as the red part in Fig. 2(b), which is further simplified as Fig. 3 to facilitate the analysis of dynamics of outer power control loop [21].

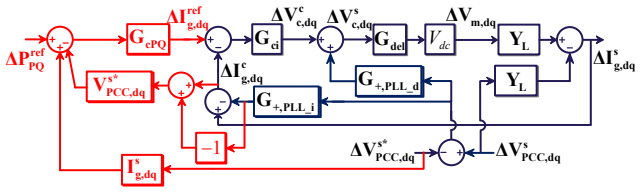

Fig. 3. Simplified complex space vector and complex transfer function-based block diagram of Fig. 1(a) further considering outer power control loop.

Similar with (11), the closed-loop response of $\mathbf{\Delta I_{g,dq}^{s}}$ with further considering outer power control loop can be derived as

$$\mathbf{\Delta I_{g,dq}^{s}} = \mathbf{G_{cl,dq}^{PCL}} \mathbf{\Delta P_{PQ}^{ref}} \underbrace{-\mathbf{Y_{cl,dq}^{CCL1}} \mathbf{\Delta V_{PCC,dq}^{s}}}_{\mathbf{CCL-related}} \cdots$$
$$\underbrace{+\mathbf{Y_{cl,dq}^{PLL1}} \mathbf{\Delta V_{PCC,dq}^{s}} - \mathbf{Y_{cl,dq}^{PLL1}} \mathbf{\Delta V_{PCC,dq}^{s*}}}_{\mathbf{PLL-related}} \cdots$$
$$\underbrace{+\mathbf{Y_{cl,dq}^{PCL1}} \mathbf{\Delta V_{PCC,dq}^{s}} + \mathbf{Y_{cl,dq}^{PCL2}} \mathbf{\Delta V_{PCC,dq}^{s*}}}_{\mathbf{PCL-related}} \quad (23)$$

where $\mathbf{G_{cl,dq}^{PCL}}$ and $\mathbf{Y_{cl,dq}^{CCL1}}$ are the closed-loop gain and current control loop-related output admittance when considering outer power control loop, respectively. In addition, $\mathbf{Y_{cl,dq}^{PLL1}}$ is the PLL-related output admittance. $\mathbf{Y_{cl,dq}^{PCL1}}$ and $\mathbf{Y_{cl,dq}^{PCL2}}$ are power control loop-related output admittance. The detailed expressions are shown as

$$\mathbf{G_{cl,dq}^{PCL}} = \frac{\mathbf{G_{cPQ}} \mathbf{T_{cl,dq}}}{1 + \mathbf{T_{cl,dq}^{PCL}}} \qquad \mathbf{Y_{cl,dq}^{CCL1}} = \frac{1 + \mathbf{T_{cl,dq}}}{1 + \mathbf{T_{cl,dq}^{PCL}}} \mathbf{Y_{cl,dq}^{CCL}}$$
$$\mathbf{Y_{cl,dq}^{PLL1}} = \frac{1 + \mathbf{T_{cl,dq}}}{1 + \mathbf{T_{cl,dq}^{PCL}}} \mathbf{Y_{cl,dq}^{PLL}}$$
$$\mathbf{Y_{cl,dq}^{PCL1}} = \frac{2\mathbf{T_{cl,dq}}}{1 + \mathbf{T_{cl,dq}^{PCL}}} \mathbf{G_{+,PLL\_i}} \mathbf{V_{PCC,dq}^{s*}} \mathbf{G_{cPQ}} \quad (24)$$
$$\mathbf{Y_{cl,dq}^{PCL2}} = \frac{\mathbf{T_{cl,dq}}}{1 + \mathbf{T_{cl,dq}^{PCL}}} (\mathbf{I_{g,dq}^{s}} - 2\mathbf{G_{+,PLL\_i}} \mathbf{V_{PCC,dq}^{s*}}) \mathbf{G_{cPQ}}$$

where $\mathbf{T_{cl,dq}^{PCL}} = (1 + \mathbf{G_{cPQ}} \mathbf{V_{PCC,dq}^{s*}}) \mathbf{T_{cl,dq}}$.

Similar with (13), when $\mathbf{\Delta P_{PQ}^{ref}} = 0$, the following equation can be obtained based on (23).

$$-\begin{bmatrix} \mathbf{\Delta I_{g,dq}^{s}} \\ \mathbf{\Delta I_{g,dq}^{s*}} \end{bmatrix} = \mathbf{Y_{\pm,dq}^{PCL,m}} \begin{bmatrix} \mathbf{\Delta V_{PCC,dq}^{s}} \\ \mathbf{\Delta V_{PCC,dq}^{s*}} \end{bmatrix} =$$
$$\begin{bmatrix} \mathbf{Y_{cl,dq}^{CCL1}} - \mathbf{Y_{cl,dq}^{PLL1}} - \mathbf{Y_{cl,dq}^{PCL1}} & \mathbf{Y_{cl,dq}^{PLL1}} - \mathbf{Y_{cl,dq}^{PCL2}} \\ \mathbf{Y_{cl,dq}^{PLL1*}} - \mathbf{Y_{cl,dq}^{PCL2*}} & \mathbf{Y_{cl,dq}^{CCL1*}} - \mathbf{Y_{cl,dq}^{PLL1*}} - \mathbf{Y_{cl,dq}^{PCL1*}} \end{bmatrix}$$
$$\begin{bmatrix} \mathbf{\Delta V_{PCC,dq}^{s}} \\ \mathbf{\Delta V_{PCC,dq}^{s*}} \end{bmatrix} \quad (25)$$

Similar with (10) and (14), the dq admittance model further considering power control loop can be derived as

$$Y_{dq}^{PCL,m} = \begin{bmatrix} Y_{dd}^{PCL} & Y_{dq}^{PCL} \\ Y_{qd}^{PCL} & Y_{qq}^{PCL} \end{bmatrix} = A_Z^{-1} \mathbf{Y_{\pm,dq}^{PCL,m}} A_Z \quad (26)$$

where

$$Y_{qq}^{PCL} = \frac{\mathbf{Y_{cl,dq}^{CCL1}} + \mathbf{Y_{cl,dq}^{CCL1*}}}{2} - \mathbf{Y_{cl,dq}^{PLL1}} - \mathbf{Y_{cl,dq}^{PLL1*}} \cdots - \frac{\mathbf{Y_{cl,dq}^{PCL1}} + \mathbf{Y_{cl,dq}^{PCL1*}} - \mathbf{Y_{cl,dq}^{PCL2}} - \mathbf{Y_{cl,dq}^{PCL2*}}}{2} \quad (27)$$

By combining (7), (15), (24) and (27), it can be seen that all of the four elements of $Y_{dq}^{PCL,m}$ are affected by power control loop dynamics. By substituting (15) and (24) into (27), the detailed expressions are shown as follows.

$$Y_{qq}^{PCL} = \frac{1 + \mathbf{T_{cl,dq}}}{1 + \mathbf{T_{cl,dq}^{PCL}}} Y_{qq}^{PLL} + \frac{\mathbf{T_{cl,dq}} \mathbf{G_{cPQ}}}{1 + \mathbf{T_{cl,dq}^{PCL}}} \frac{P^{ref}}{V_{PCC,d}^{s}} \cdots (1 - 2G_{PLL} V_{PCC,d}^{s}) \quad (28)$$

Similar with (16), the q-axis component of the dq impedance model when further considering outer power control loop can be calculated as

$$Z_{qq}^{PCL} = -\frac{G_{cPQ} G_{ci} G_{del} I_{g,q}^{ref} C + BD}{A} \quad (29)$$

where the detailed expressions of A, B, C and D are shown as

$$A = \frac{G_{cPQ} G_{ci}^2 G_{del}^2 (G_{cPQ} + G_{PLL}) [(P^{ref})^2 + (Q^{ref})^2]}{(V_{PCC,d}^{s})^2} + \cdots$$
$$G_{PLL} G_{del} [\frac{0.5 V_{dc} G_{ci} P^{ref} + (V_{PCC,d}^{s})^2 - \omega_1 L_f Q^{ref}}{0.5 V_{dc} V_{PCC,d}^{s}}] + \cdots$$
$$\frac{G_{PLL} G_{cPQ} G_{ci} G_{del}^2 P^{ref}}{0.5 V_{dc}} - 1$$
$$B = L_f s + \frac{G_{del} V_{dc} G_{ci} (1 + G_{cPQ} V_{PCC,d}^{s})}{2}$$
$$C = \omega_1 L_f \qquad D = 1 + \frac{G_{ci} G_{cPQ} G_{del} P^{ref}}{V_{PCC,d}^{s}} \quad (30)$$

IV. Proposed DQ Impedance Reshaping Method for Low-Frequency Stability Improvement

In this section, the existing feed-forward control loop-based dq impedance reshaping method for current-controlled GCI is first explained, where the selection of the feed-forward coefficient is also introduced. On its basis, the feed-forward control loop-based dq impedance reshaping method is further extended for power-controlled GCI.

A. Low-Frequency Impedance Characteristics of Inner Current Control Loop and PLL

Based on (10), low-frequency impedance model of Z_{qq}^{CCL} can be approximated as

$$Z_{qq}^{CCL} = k_{pi} V_{dc} \cos(1.5\omega T_s) + j(L_f \omega - k_{pi} V_{dc} \sin(1.5\omega T_s)) \approx k_{pi} V_{dc} + j L_f \omega \quad (31)$$

Then, the magnitude and phase angle of Z_{qq}^{CCL} in low-frequency range can be calculated based on (31), shown as

$$|Z_{qq}^{CCL}| = \sqrt{(k_{pi} V_{dc})^2 + (L_f \omega)^2}$$
$$\angle Z_{qq}^{CCL} = \arctan \frac{L_f \omega}{k_{pi} V_{dc}} \in (0, 90^o) \quad (32)$$

It can be seen that $\angle Z_{qq}^{CCL}$ belongs to $(0^o, 90^o)$ in low-frequency range, i.e., low-frequency instability phenomena will not happen if only inner current control loop is considered.

Then, G_{qq}^{PLL} is defined as

$$G_{qq}^{PLL} = 1 - (V_{c,d}^{s} + I_{g,d}^{s} G_{ci}) G_{PLL} G_{del} V_{dc} = real(G_{qq}^{PLL}) + imag(G_{qq}^{PLL}) \quad (33)$$

where $real(G_{qq}^{PLL}) < 0$ and $imag(G_{qq}^{PLL}) \approx 0^+$, since $G_{PLL} \approx 1/V_{PCC,d}^{s}$ and $G_{del} \approx 1$ in low-frequency range.

Therefore,

$$|Z_{qq}^{PLL}| = |Z_{qq}^{CCL}| / |G_{qq}^{PLL}| < |Z_{qq}^{CCL}|$$
$$\angle Z_{qq}^{PLL} = \angle Z_{qq}^{CCL} - \angle G_{qq}^{PLL} \approx \arctan \frac{L_f \omega}{k_{pi} V_{dc}} \cdots -180^o \in (-180^o, -90^o) \quad (34)$$

It can be seen from (32) and (34) that, the PLL tends to decrease the magnitude of q-axis impedance component in low-frequency range, and decrease the phase angle into $(-180^o, -90^o)$, which may lead to low-frequency instability phenomena.

B. Existing Q-Axis Impedance Reshaping Method for Current-Controlled GCI

The feed-forward control loop-based q-axis impedance reshaping method for current-controlled GCI has been well documented in [16], [22], [23]. The core idea is explained here based on the derived complex transfer function-based dq impedance models in Sections II and III.

The feed-forward control loop is implemented as the dashed brown line in Fig. 2(a) (The red part for outer power control loop is not considered here.). The effect of $K_{ff}^{m} = [K_{ff}, 0; 0, K_{ff}]$ on Y_{qq}^{PLL} is defined as Y_{qqff}^{PLL} which can be calculated as

$$Y_{qqff}^{PLL} = \frac{K_{ff} G_{ci} G_{del} V_{dc}}{L_f s + G_{ci} G_{del} V_{dc}} \quad (35)$$

In addition, the effect of PLL dynamics on Y_{qq}^{PLL} has been derived in (15). For simplification, the coupling effect between d-axis and q-axis is ignored, which can be satisfied when $I_{g,q}^{s} = 0$ [23]. Therefore,

$$Y_{qqPLL}^{PLL} = -\mathbf{Y_{cl,dq}^{PLL}} - \mathbf{Y_{cl,dq}^{PLL*}} \approx -\frac{(V_{c,d}^{s} + I_{g,d}^{s} G_{ci}) G_{PLL} G_{del} V_{dc}}{L_f s + G_{ci} G_{del} V_{dc}} \quad (36)$$

To eliminate the negative effect of PLL dynamics on low-frequency stability, Y_{qqff}^{PLL} and Y_{qqPLL}^{PLL} should be canceled out, i.e. [23],

$$Y_{qqff}^{PLL} + Y_{qqPLL}^{PLL} = 0 \quad (37)$$

K_{ff} can be calculated from (35)-(37), shown as

$$K_{ff} = G_{PLL} (\frac{V_{c,d}^{s}}{G_{ci}} + I_{g,d}^{s}) \approx \frac{1}{V_{PCC,d}^{s}} (\frac{V_{c,d}^{s}}{k_{pi}} + I_{g,d}^{s}) \quad (38)$$

C. Proposed Q-Axis Impedance Reshaping Method for Power-Controlled GCI

When $Q^{ref}=0$, the phase angle of Z_{qq}^{PCL} can be calculated as [21]

$$\angle Z_{qq}^{PCL}=\arctan\frac{(\Gamma_1+\Gamma_3P^{ref})\omega}{\Gamma_2+\Gamma_4P^{ref}}-180^o \tag{39}$$

where Γ_1, Γ_2, Γ_3 and Γ_4 are shown as

$$\begin{aligned}&\Gamma_1=L_f \qquad \Gamma_2=\frac{G_{del}V_{dc}G_{ci}(1+G_{cPQ}V_{PCC,d}^s)}{2}\\&\Gamma_3=\frac{G_{ci}G_{cPQ}G_{del}L_f}{V_{PCC,d}^s}\\&\Gamma_4=\frac{G_{ci}^2G_{cPQ}G_{del}^2V_{dc}(1+G_{cPQ}V_{PCC,d}^s)}{2V_{PCC,d}^s}\end{aligned} \tag{40}$$

If $k_{pPQ}>\frac{1}{V_{PCC,d}^s}$, which is commonly satisfied, (41) holds.

$$\frac{L_f\omega}{k_{pi}V_{dc}}/\frac{(\Gamma_1+\Gamma_3P^{ref})\omega}{\Gamma_2+\Gamma_4P^{ref}}\approx\frac{1}{2}(1+k_{pPQ}V_{PCC,d}^s)>1 \tag{41}$$

It can be seen from (34) and (39) that,

$$\arctan\frac{L_f\omega}{k_{pi}V_{dc}}>\arctan\frac{(\Gamma_1+\Gamma_3P^{ref})\omega}{\Gamma_2+\Gamma_4P^{ref}}\Rightarrow\angle Z_{qq}^{PLL}>\angle Z_{qq}^{PCL} \tag{42}$$

(42) shows that when further considering outer power control loop, the phase angle of the q-axis impedance component is further decreased, which indicates that the designed K_{ff} for the current-controlled GCI should be adjusted.

By substituting (15) into (28), and assuming $\frac{\mathbf{T_{cl,dq}}}{1+\mathbf{T_{cl,dq}}}=1$ in low-frequency range, (28) can be reformulated as

$$\begin{aligned}Y_{qq}^{PCL}=&\frac{1}{1+\mathbf{G_{cPQ}V_{PCC,dq}^{s*}}}(\frac{\mathbf{Y_{cl,dq}^{CCL}+Y_{cl,dq}^{CCL*}}}{2}-\mathbf{Y_{cl,dq}^{PLL}}-\\&...\mathbf{Y_{cl,dq}^{PLL*}}+\frac{\mathbf{G_{cPQ}}P^{ref}}{V_{PCC,d}^s}(1-2G_{PLL}V_{PCC,d}^s))\end{aligned} \tag{43}$$

Similar with (36), the effects of PLL dynamics and outer power control loop on Y_{qq}^{PCL} can be defined based on (37) and (43), shown as

$$\begin{aligned}&Y_{qqPLL\_PCL}^{PCL}=\frac{1}{1+\mathbf{G_{cPQ}V_{PCC,dq}^{s*}}}(-\mathbf{Y_{cl,dq}^{PLL}}-\mathbf{Y_{cl,dq}^{PLL*}}...\\&+\frac{\mathbf{G_{cPQ}}P^{ref}}{V_{PCC,d}^s}(1-2G_{PLL}V_{PCC,d}^s))=\frac{1}{1+k_{pPQ}V_{PCC,d}^s}...\\&(-Y_{qqff}^{PLL}+\frac{k_{pPQ}P^{ref}}{V_{PCC,d}^s}(1-2G_{PLL}V_{PCC,d}^s))\end{aligned} \tag{44}$$

On the other hand, the effect of the feed-forward control loop with coefficient $K_{ff1}^m=[K_{ff1},0;0,K_{ff1}]$ in Fig. 2(a) on q-axis impedance component can be de calculated as (The red part for outer power control loop is considered here.)

$$Y_{qqff1}^{PLL}=\frac{K_{ff1}G_{ci}G_{del}V_{dc}}{(1+k_{pPQ}V_{PCC,d}^s)(L_fs+G_{ci}G_{del}V_{dc})} \tag{45}$$

Similar with (37), to eliminate the negative effects of both PLL dynamics and outer power control loop on low-frequency stability, Y_{qqff1}^{PLL} and $Y_{qqPLL\_PCL}^{PCL}$ should be canceled out, i.e.,

$$Y_{qqff1}^{PLL}+Y_{qqPLL\_PCL}^{PCL}=0 \tag{46}$$

K_{ff1} can be calculated from (44)-(46), shown as

$$\begin{aligned}K_{ff1}&=K_{ff}-\frac{k_{pPQ}P^{ref}(1-2G_{PLL}V_{PCC,d}^s)(1+\frac{L_fs}{G_{ci}V_{dc}})}{V_{PCC,d}^s}\\&\approx K_{ff}+\frac{k_{pPQ}P^{ref}}{V_{PCC,d}^s}=K_{ff}+k_{pPQ}I_{g,d}^s\end{aligned} \tag{47}$$

It can be seen from (47) that, the coefficient of the designed feed-forward control loop K_{ff1} when further considering outer power control loop is larger than the coefficient of the designed feed-forward control loop K_{ff} when only considering inner current control loop and PLL.

V. Simulation Verification

In this section, the effectiveness of the proposed q-axis impedance component reshaping method for low-frequency stability improvement of power-controlled GCI is verified by frequency scanning and time-domain simulation in Matlab/Simulink environment.

A. Frequency Scanning Results of the Q-Axis Impedance Component

The circuit and controller parameters of the GCI in Fig. 1(a) are shown in Table I. Fig. 4(a) shows the Bode diagrams of Z_{qq}^{PLL} with different K_{ff} when the outer power control loop is not considered. In addition, $I_{g,d}^{ref}=2.0$ kA and $I_{g,q}^{ref}=0$. It can be seen that, by increasing K_{ff}, the phase angle in low-frequency range is boosted, and the non-passive region is narrowed. Specifically, the non-passive frequency range is narrowed to (0, 4.5 Hz) when $K_{ff}=1.7391$. When K_{ff} is 0 or 0.0435, the phase angle difference at the magnitude interaction point A (14.8 Hz) of the q-axis impedance components of GCI and the weak grid is $84.25-(-96.36)=180.61^o$ and $84.25-(-96.00)=180.25^o$, respectively. Therefore, the system is unstable, and will oscillate at 14.8 Hz. In addition, when K_{ff} is 0.1739 or 0.4348, the phase angle difference at the magnitude interaction point A (14.8 Hz) of the q-axis impedance components of GCI and the weak grid is $84.25-(-89.55)=173.80^o$ and $84.25-(-79.77)=164.02^o$, respectively. Therefore, the system becomes stable at the two cases. When K_{ff} is further increased to 0.6957 or 1.7391, the phase angle difference at the magnitude interaction point B (14.3 Hz) or C (14 Hz) of the q-axis impedance components of GCI and the weak grid is $85.75-(-71.91)=157.66^o$ and $86.65-(-50.04)=136.69^o$, respectively, which indicates that the system is stable under the two cases, and the phase margin is increased with a large K_{ff}.

On the other hand, Fig. 4(b) shows the Bode diagrams of Z_{qq}^{PCL} with different K_{ff1} when the outer power control loop is considered. In addition, $P^{ref}=2.0$ MW and $Q^{ref}=0$. It can be seen that, by increasing K_{ff1}, the phase angle in

TABLE I
CIRCUIT AND CONTROLLER PARAMETERS OF THE GCI

Parameter	Value
DC-link voltage V_{dc}	1150 V
Grid fundamental frequency f_1	50 Hz
Inverter side filter inductance L_{f1}	263 μH
Grid side filter inductance L_{f2}	200 μH
Filter capacitance C_f	40 μF
Switching frequency f_{swit}	2.5 kHz
Sampling frequency f_{samp}	2.5 kHz
Grid Vrms (phase-to-phase) V_g	575 V
Proportional gain of power controller k_{pPQ}	2.7454e-05
Integral gain of power controller k_{iPQ}	0.0165
Proportional gain of current controller k_{pi}	5.4908e-04
Integral gain of current controller k_{ii}	0.3295
Proportional gain of PLL k_{ppll}	20
Integral gain of PLL k_{ipll}	200

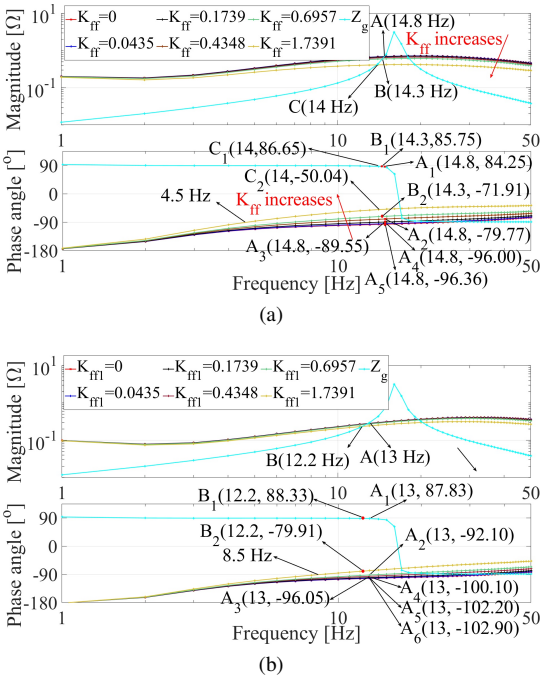

Fig. 4. Bode diagrams of q-axis impedance component. (a) Bode diagrams of Z_{qq}^{PLL} with different K_{ff}. (b) Bode diagrams of Z_{qq}^{PCL} with different K_{ff1}

low-frequency range is boosted, and the non-passive region is narrowed. Specifically, the non-passive frequency range is narrowed to (0, 8.5 Hz) when $K_{ff1} = 1.7391$. By comparing the two yellow lines in Figs. 4(a) and (b), it can be seen that, with the same coefficient of the feed-forward control loop, the non-passive region of the power-controlled GCI is wider than that of the current-controlled GCI, which verifies the correctness of the theoretical analysis in (42).

When K_{ff1} is 0, 0.0435, 0.1739 or 0.4348, the phase angle difference at the magnitude interaction point A (13 Hz) of the q-axis impedance components of GCI and the weak grid is $87.83-(-102.90) = 190.73^o$, $87.83-(-102.20) = 190.03^o$, $87.83-(-100.10) = 187.93^o$ or $87.83-(-96.05) = 183.88^o$, respectively. Therefore, the system is unstable under the four

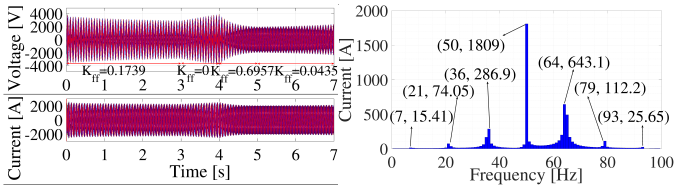

(a) (b)

Fig. 5. Time-domain simulation results of current-controlled GCI with different K_{ff}. (a) Three-phase voltages and currents. (b) FFT of three-phase currents between 3 s and 4 s.

cases, and will oscillate at 13 Hz. In addition, when K_{ff} is further increased to 0.6957 or 1.7391, the phase angle difference at the magnitude interaction point A (13 Hz) or B (12.2 Hz) of the q-axis impedance components of GCI and the weak grid is $87.83-(-92.10) = 179.93^o$ and $87.83-(-79.91) = 167.74^o$, respectively, which indicates that the system is stable under the two cases, and the phase margin is increased with a large K_{ff1}.

It can be seen from Figs. 4(a) and (b) that, the minimum coefficient of the feed-forward control loop of the current-controlled GCI for enforcing low-frequency stability is 0.1739, whereas the minimum coefficient of the feed-forward control loop of the power-controlled GCI for enforcing low-frequency stability is increased to 0.6957, which indicates the required minimum coefficient of the power-controlled GCI is higher than that of the current-controlled GCI. The correctness of the theoretical analysis in (47) is thus validated.

Fig. 5(a) shows the time-domain simulation results of three-phase voltages and currents of the current-controller GCI with different K_{ff}. It can be seen that, the system is stable before 3 s when $K_{ff} = 0.1739$. In addition, the system becomes unstable between 3 s and 4 s when $k_{ff} = 0$. When K_{ff} is increased to 0.6957 at 4 s, the system becomes stable again. Furthermore, the system becomes unstable again when K_{ff} is decreased to 0.0435 at 5 s. In addition, the frequency spectrum of the three-phase currents between 3 s and 4 s is shown in Fig. 5(b), where the oscillation mainly occurs at 64 Hz and 36 Hz. The time-domain simulation results and FFT analysis agree with the theoretical analysis results in Fig. 4(a).

Fig. 6(a) shows the time-domain simulation results of three-phase voltages and currents of the power-controller GCI with different K_{ff1}. It can be seen that, the system is stable before 2 s when $K_{ff1} = 0.6957$. In addition, the system becomes unstable between 2 s and 2.4 s when $k_{ff1} = 0$. When K_{ff1} is increased to 1.7391 at 2.4 s, the system becomes stable again. Furthermore, the system becomes unstable again when K_{ff1} is decreased to 0.1739 at 3.4 s. In addition, the frequency spectrum of the three-phase currents between 5 s and 6 s is shown in Fig. 6(b), where the oscillation mainly occurs at 65 Hz and 35 Hz. The time-domain simulation results and FFT analysis agree with the theoretical analysis results in Fig. 4(b).

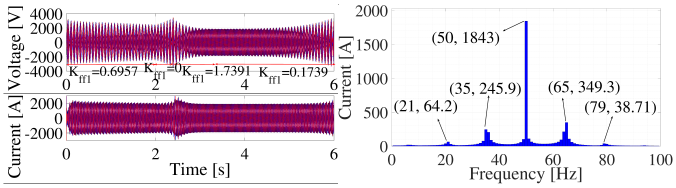

(a) (b)

Fig. 6. Time-domain simulation results of power-controlled GCI with different K_{ff1}. (a) Three-phase voltages and currents. (b) FFT of three-phase currents between 5 s and 6 s.

VI. Conclusion

The passivity of the GCI in low-frequency range can be forced based on feed-forward control loop. The theoretical analysis results in this paper show that the conventional feed-forward control loop designed for the current-controlled GCI cannot guarantee the passivity of the power-controlled GCI in low-frequency range anymore. Based on the conventional q-axis impedance component reshaping method, this paper presents a modified feed-forward control loop design method of power-controlled GCI, where the coefficient is adjusted based on the power controller parameters. Both frequency scanning results and time-domain simulation results verify the effectiveness of the modified q-axis impedance component reshaping method for low-frequency stability improvement.

References

[1] F. Blaabjerg, Z. Chen, and S. B. Kjaer, "Power electronics as efficient interface in dispersed power generation systems," *IEEE Trans. Power Electron.*, vol. 19, no. 5, pp. 1184–1194, Sep. 2004.

[2] X. Wang and F. Blaabjerg, "Harmonic stability in power electronic-based power systems: Concept, modeling, and analysis," *IEEE Trans. Smart Grid*, vol. 10, no. 3, pp. 2858–2870, May 2019.

[3] W. Zhou, Y. Wang, and Z. Chen, "Impedance-decoupled modelling method of multi-port transmission network in inverter-fed power plant," *IEEE Trans. Ind. Appl.*, vol. 56, no. 1, pp. 611–621, Jan./Feb. 2020.

[4] F. Blaabjerg, R. Teodorescu, M. Liserre, and A. V. Timbus, "Overview of control and grid synchronization for distributed power generation systems," *IEEE Trans. Ind. Electron.*, vol. 53, no. 5, pp. 1398–1409, Oct. 2006.

[5] L. Harnefors, M. Bongiorno, and S. Lundberg, "Input-admittance calculation and shaping for controlled voltage-source converters," *IEEE Trans. Ind. Electron.*, vol. 54, no. 6, pp. 3323–3334, Dec. 2007.

[6] T. Messo, J. Jokipii, A. Mäkinen, and T. Suntio, "Modeling the grid synchronization induced negative-resistor-like behavior in the output impedance of a three-phase photovoltaic inverter," in *Proc. IEEE 2013 4th IEEE International Symposium on Power Electronics for Distributed Generation Systems (PEDG)*, pp. 1–7.

[7] J. Z. Zhou, H. Ding, S. Fan, Y. Zhang, and A. M. Gole, "Impact of short-circuit ratio and phase-locked-loop parameters on the small-signal behavior of a VSC-HVDC converter," *IEEE Trans. Power Del.*, vol. 29, no. 5, pp. 2287–2296, Oct. 2014.

[8] D. Dong, B. Wen, D. Boroyevich, P. Mattavelli, and Y. Xue, "Analysis of phase-locked loop low-frequency stability in three-phase grid-connected power converters considering impedance interactions," *IEEE Trans. Ind. Electron.*, vol. 62, no. 1, pp. 310–321, Jan. 2014.

[9] B. Wen, D. Boroyevich, R. Burgos, P. Mattavelli, and Z. Shen, "Analysis of DQ small-signal impedance of grid-tied inverters," *IEEE Trans. Power Electron.*, vol. 31, no. 1, pp. 675–687, Jan. 2016.

[10] Y. Xia, Y. Peng, P. Yang, Y. Li, and W. Wei, "Different influence of grid impedance on low- and high-frequency stability of PV generators," *IEEE Trans. Ind. Electron.*, vol. 66, no. 11, pp. 8498–8508, Nov. 2019.

[11] W. Zhou, R. E. Torres, Y. Wang, and Z. Chen, "A gray-box hierarchical oscillatory instability source identification method of multiple-inverter-fed power systems," *IEEE J. Emerg. Sel. Topics Power Electron.*, Early Access, doi: 10.1109/JESTPE.2020.2992225.

[12] M. Cespedes and J. Sun, "Adaptive control of grid-connected inverters based on online grid impedance measurements," *IEEE Trans. Sustain. Energy*, vol. 5, no. 2, pp. 516–523, 2014.

[13] M. Amin and M. Molinas, "A gray-box method for stability and controller parameter estimation in HVDC-connected wind farms based on nonparametric impedance," *IEEE Trans. Ind. Electron.*, vol. 66, no. 3, pp. 1872–1882, Mar. 2019.

[14] M. Davari and Y. A.-R. I. Mohamed, "Robust vector control of a very weak-grid-connected voltage-source converter considering the phase-locked loop dynamics," *IEEE Trans. Power Electron.*, vol. 32, no. 2, pp. 977–994, Feb. 2017.

[15] S. Zhou, X. Zou, D. Zhu, L. Tong, Y. Zhao, Y. Kang, and X. Yuan, "An improved design of current controller for LCL-type grid-connected converter to reduce negative effect of PLL in weak grid," *IEEE J. Emerg. Sel. Topics Power Electron.*, vol. 6, no. 2, pp. 648–663, Jun. 2018.

[16] D. Yang, X. Wang, F. Liu, K. Xin, Y. Liu, and F. Blaabjerg, "Symmetrical PLL for SISO impedance modeling and enhanced stability in weak grids," *IEEE Trans. Power Electron.*, vol. 35, no. 2, pp. 1473–1483, Feb. 2020.

[17] K. M. Alawasa, Y. A.-R. I. Mohamed, and W. Xu, "Active mitigation of subsynchronous interactions between PWM voltage-source converters and power networks," *IEEE Trans. Power Electron.*, vol. 29, no. 1, pp. 121–134, Jan. 2014.

[18] K. M. Alawasa and Y. A.-R. I. Mohamed, "A simple approach to damp SSR in series-compensated systems via reshaping the output admittance of a nearby VSC-based system," *IEEE Trans. Ind. Electron.*, vol. 62, no. 5, pp. 2673–2682, May 2015.

[19] J. Xu, S. Bian, Q. Qian, J. Kan, and S. Xie, "Suppression of harmonics and instabilities of single-phase inverters caused by delay-based phase-locked loop in the weak grid," in *Proc. IEEE 2019 10th International Conference on Power Electronics and ECCE Asia (ICPE 2019-ECCE Asia)*, pp. 1–6.

[20] W. Zhou, Y. Wang, D. Liu, and Z. Chen, "Optimization of active and reactive power dispatch among multi-paralleled grid-connected inverters considering low-frequency stability," in *Proc. IEEE IECON 2019-45th Annual Conference of the IEEE Industrial Electronics Society*, pp. 4383–4389.

[21] W. Zhou, Y. Wang, R. E. Torres-Olguin, and Z. Chen, "Effect of reactive power characteristic of offshore wind power plant on low-frequency stability," *IEEE Trans. Energy Convers.*, vol. 35, no. 2, pp. 837–853, Jun. 2020.

[22] X. Zhang, D. Xia, Z. Fu, G. Wang, and D. Xu, "An improved feedforward control method considering PLL dynamics to improve weak grid stability of grid-connected inverters," *IEEE Trans. Ind. Appl.*, vol. 54, no. 5, pp. 5143–5151, Sep./Oct. 2018.

[23] J. Fang, X. Li, H. Li, and Y. Tang, "Stability improvement for three-phase grid-connected converters through impedance reshaping in quadrature-axis," *IEEE Trans. Power Electron.*, vol. 33, no. 10, pp. 8365–8375, Oct. 2018.

[24] R. Luhtala, T. Reinikka, H. Alenius, T. Roinila, and T. Messo, "Adaptive method for control tuning of grid-connected inverter based on grid measurements during start-up," in *Proc. IEEE 2019 18th European Control Conference (ECC)*, pp. 417–422.

[25] L. Harnefors, "Modeling of three-phase dynamic systems using complex transfer functions and transfer matrices," *IEEE Trans. Ind. Electron.*, vol. 54, no. 4, pp. 2239–2248, Aug. 2007.

[26] X. Wang, L. Harnefors, and F. Blaabjerg, "Unified impedance model of grid-connected voltage-source converters," *IEEE Trans. Power Electron.*, vol. 33, no. 2, pp. 1775–1787, Feb. 2018.

[27] A. Rygg, M. Molinas, C. Zhang, and X. Cai, "On the equivalence and impact on stability of impedance modeling of power electronic converters in different domains," *IEEE J. Emerg. Sel. Topics Power Electron.*, vol. 5, no. 4, pp. 1444–1454, Dec. 2017.